

Formation of Silica Nanoparticles in Microemulsions

Kim S. Finnie,* John R. Bartlett, Christophe J. A. Barbé, and Linggen Kong

Australian Nuclear Science and Technology Organisation, PMB 1, Menai NSW 2234 Australia

Received August 17, 2006. In Final Form: December 7, 2006

Silica nanoparticles for controlled release applications have been produced by the reaction of tetramethylorthosilicate (TMOS) inside the water droplets of a water-in-oil microemulsion, under both acidic (pH 1.05) and basic (pH 10.85) conditions. In-situ FTIR measurements show that the addition of TMOS to the microemulsion results in the formation of silica as TMOS, preferentially located in the oil phase, diffuses into the water droplets. Once in the hydrophilic domain, hydrolysis occurs rapidly as a result of the high local concentration of water. Varying the pH of the water droplets from 1.05 to 10.85, however, considerably slows the hydrolysis reaction of TMOS. The formation of a dense silica network occurs rapidly under basic conditions, with IR indicating the slower formation of more disordered silica in acid. SAXS analysis of the evolving particles shows that ~ 11 nm spheres are formed under basic conditions; these are stabilized by a water/surfactant layer on the particle surface during formation. Under acidic conditions, highly uniform ~ 5 nm spheres are formed, which appear to be retained within the water droplets (~ 6 nm diameter) and form an ordered micelle nanoparticle structure that exhibits sufficient longer-range order to generate a peak in the scattering at $q \approx 0.05 \text{ \AA}^{-1}$. Nitrogen adsorption analysis reveals that high surface area ($510 \text{ m}^2/\text{g}$) particles with an average pore size of 1 nm are formed at pH 1.05. In contrast, base synthesis results in low surface area particles with negligible internal porosity.

Introduction

Monodisperse silica nanoparticles with tailored particle size (50–250 nm) and porosity have been proposed as suitable vehicles for controlled release applications, and, in particular, drug delivery.¹ Because amorphous silica particles (in contrast to crystalline silica) are biologically inert and biocompatible² and are chemically and mechanically resistant, they present an interesting alternative to more common organic delivery systems such as liposomes, micelles, dendrimers, and polymeric particles.³ The requirements for a successful delivery system are precise control of the size for targeting specific organs or avoidance of clearing by the immune system as well as control of the release rate, which is generally achieved by tailoring the particles' internal structure, composition, or physical properties. In the case of silica nanoparticles, this is achieved by coupling sol–gel chemistry with a microemulsion process, which enables independent control of the particle size and microstructure, thus providing a means of controlling the release rates of encapsulated species and targeting tumors.⁴

Spherical silica particles in the nominated size range may be conveniently synthesized by the addition of silicon alkoxide, typically tetraethylorthosilicate (TEOS), to a reverse water-in-oil microemulsion.⁵ The diffusion of the alkoxide into the water droplets results in hydrolysis of the alkoxide and formation of oxy-hydroxy-silicate species and alcohol. We have found that

hydrophilic drug molecules located inside the water droplets prior to addition of the silicon alkoxide can be effectively encapsulated inside the nanoparticles as they form in the microemulsion. The ensuing release rate of the drug from the nanoparticles is dependent upon the pore structure of the nanoparticles, which is determined by a number of factors, including the water/alkoxide molar ratio, the pH, and the kinetics of hydrolysis and condensation.⁴ A complicating factor is that certain drugs are stable over a limited pH range, which may not correspond to the optimum pH for rapid hydrolysis and condensation reactions of the alkoxide.

The hydrolysis and condensation reactions of alkoxy-silicates have been discussed in detail by Brinker and Scherer.⁶ A comparison of the hydrolysis rates of TEOS with the corresponding methoxysilicate TMOS shows that the hydrolysis rates of TMOS under both acidic and basic conditions are considerably faster because of the retarding effect of the bulkier ethoxide group.⁶ TMOS is the preferred precursor for drug encapsulation, therefore, as a result of the reduced reaction time.

Whereas reverse micelles have been used for the production of ceramic nanospheres for some time, the mechanism for nanoparticle formation has been investigated only for the base-catalyzed hydrolysis of TEOS. Kinetic studies of the formation of silica nanoparticles in microemulsions⁷ and in alcohol (Stober process)⁸ have been conducted, the latter using SAXS and dynamic light scattering to determine the size of the primary particles produced. A significant number of drug molecules selected for encapsulation have proved to be stable only under acidic conditions. However, there has been some difficulty in obtaining particles from an acid-catalyzed reaction in the microemulsion. This was assumed to be due to the slower condensation reactions at low pH (1.05) and has been addressed

* Corresponding author. E-mail: ksf@ansto.gov.au.

(1) Barbé, C.; Bartlett, J.; Kong, L.; Finnie, K.; Lin, H. Q.; Larkin, M.; Calleja, S.; Bush, A.; Calleja, G. *Adv. Mater.* **2004**, *16*, 1959.

(2) (a) Lia, W.; Garino, J.; Ducheyne, P. In *Bioceramics II*; Legeros, R. Z., Legeros, J. P., Eds.; World Scientific Publishing: New York, 1998, p 383. (b) Lai, W.; Garino, J.; Ducheyne, P. *Biomaterials* **2002**, *23*, 213.

(3) (a) *Sustained-Release Injectable Products*; Senior, J., Radomsky, M., Eds.; Interpharm Press: Denver, 2000. (b) Wise, D. L. *Handbook of Pharmaceutical Controlled Release Technology*; Marcel Dekker: New York, 2000.

(4) Barbé, C. J. A.; Bartlett, J.; PCT Patent WO 01/62232, 2001.

(5) (a) Yamauchi, H.; Ishikawa, T.; Kondo, S. *Colloids Surf.* **1989**, *37*, 71. (b) Osseo-Asare, K.; Arriagada, F. J. *Colloids Surf.* **1990**, *50*, 321. (c) Chang, C. L.; Fogler, H. S. *Langmuir* **1997**, *13*, 3295. (d) Osseo-Asare, K. In *Handbook of Microemulsion Science and Technology*; Kumar, P., Mittal, K. L., Eds.; Marcel Dekker, New York, 1999; p 549. (e) Santra, S.; Zhang, P.; Wang, K.; Tapecc, R.; Tan, W. *Anal. Chem.* **2001**, *73*, 4988.

(6) Brinker, C. J.; Scherer, G. W. *Sol-Gel Science*; Academic Press: New York, 1990.

(7) Osseo-Asare, K.; Arriagada, F. J. *J. Colloid Interface Sci.* **1999**, *218*, 68.

(8) Green, D. L.; Lin, J. S.; Lam, Y.-F.; Hu, M. Z.-C.; Schaefer, D. W.; Harris, M. T. *J. Colloid Interface Sci.* **2003**, *266*, 346.

here by the addition of fluoride⁹ to catalyze the condensation of silica in the microemulsion.

To understand and control nanoparticle formation better and hence optimize the yield and release rate of encapsulated drugs, we have undertaken a study of the kinetics and mechanism of nanoparticle formation in the NP-5/cyclohexane microemulsion system under both acidic (pH 1.05) and basic (pH 10.85) conditions, with the pH selected to optimize the hydrolysis rate of TMOS. Fourier transform infrared (FTIR) spectroscopy was used to follow the hydrolysis of TMOS, and small-angle X-ray scattering (SAXS) measurements were used to detect the formation of scattering particulates. Surface area and porosity measurements were conducted to determine the size of the particulate building blocks.

Experimental Methods

Samples. Cyclohexane, acetonitrile, tetramethylorthosilicate (TMOS) and polyoxyethylene (5) nonylphenyl ether ($C_9H_{19}-C_6H_4-(OCH_2CH_2)_nOH$, $n \approx 5$, NP-5) were obtained from Sigma-Aldrich and were used as received. Microemulsions were generated by dissolving the non-ionic surfactant NP-5 in cyclohexane and adding either dilute nitric acid or an ammonia solution, respectively, in a 6:1 molar ratio of water/surfactant. Nanoparticle synthesis was conducted inside the microemulsion water droplets at pH 1.05 and 10.85.

Synthesis Procedure. NP-5 (2.64 g) was mixed with cyclohexane (30 mL) and stirred at ambient temperature (300 rpm) until dissolved. Nitric acid (0.65 mL) diluted to pH 1.05 or ammonia solution diluted to pH 10.85 was added to the respective surfactant solutions and stirred until optically transparent. In the case of the acid synthesis, the dilute acid also contained sodium fluoride (1.04 mg). Finally, TMOS (0.364 mL) was added to the microemulsions with continued stirring.

Characterization. The most diagnostic infrared bands are the antisymmetric Si–O stretch of the TMOS ($Si-O$)₄ unit at 830 cm^{-1} , the antisymmetric Si–O stretch of the emerging silicate species (1000–1200 cm^{-1}), and the C–O stretch of methanol at 1028 cm^{-1} . The absorption of surfactant and cyclohexane in this spectral region presents a problem due to the comparatively low concentration of the silicate species, and it is necessary to subtract these bands from the spectrum. To do this accurately, we measured attenuated total reflectance (ATR) spectra in which the depth of penetration, d_p , of the evanescent IR beam into a sample on the surface of an ATR prism is given by

$$d_p = \frac{\lambda}{2\pi n_p} \sqrt{(\sin^2 \theta - n_{sp}^2)}$$

and

$$n_{sp} = \frac{n_s}{n_p}$$

where λ is the wavelength of radiation, n_p is the refractive index of the ATR prism, n_s is the refractive index of the sample, and θ is the angle of incidence of the beam at the surface of the prism.¹⁰ Thus for a given wavelength and prism, the penetration depth is dependent only on the refractive index of the solution, which is largely determined by the solvent and is thus easily reproducible. FTIR spectra (4000–530 cm^{-1}) were recorded using a Digilab FTS-40 spectrometer equipped with a linearized MCT detector. Each spectrum was an average of 1024 scans, with a resolution of 4 cm^{-1} . The ATR element consisted of a 45° single reflection ZnSe crystal (Harrick). A 0.2 mL aliquot of the microemulsion was withdrawn for each

measurement. An initial spectrum of the surfactant/solvent/water microemulsion served as a reference for the spectra measured at timed intervals following the addition of TMOS to the system. The spectra were not corrected for wavelength dependence because only the variation in intensity of each band with time was of interest. Spectral data were manipulated using Win-IR v.4 (Digilab), including curve fitting of bands in the spectral region of 800–1250 cm^{-1} using mixed Gaussian/Lorentzian functions to determine band areas.

The SAXS instrumentation used in this work has been described previously.¹¹ Briefly, Cu K α radiation from a rotating anode source was focused onto the samples, which were held in 1 mm silica capillaries at ambient temperature and pressure. Data were typically acquired for 2 h over a q range of 0.01 to 0.4 \AA^{-1} using a 1D wire detector and were calibrated against the scattering of pure water and cyclohexane to obtain intensities in absolute units. All fits were undertaken using a nonlinear least-squares algorithm to optimize the fits, with particle size and polydispersity used as variable parameters. Chi test values of around 1 were obtained, reflecting statistically relevant fits to the data. The internal consistency of each data set was verified by calculating the X-ray absorptivity of the samples from their known compositions and standard X-ray absorptivities of each element and then using the Beer–Lambert law to obtain the apparent sample thickness from the measured transmission. This apparent thickness was then compared to the nominal sample thickness to ensure internal consistency.

The pore size, pore volume, and surface area were measured using an ASAP 2010 nitrogen sorption instrument (Micromeritics). The samples were dried at 60 °C under vacuum prior to measurement. The DFT model¹² was applied to the adsorption branch of the isotherm, assuming cylindrically shaped pores. The BET surface area was calculated using a five-point regression.

Results

Infrared. The full vibrational spectrum of TMOS has been analyzed in detail, and the reported assignments are used here.¹³ The wavelength range of 1300–750 cm^{-1} contains the main TMOS vibrations as well as the Si–O vibrations of the oxyhydroxy-silicate species formed as TMOS is hydrolyzed. The main bands of interest are the triply degenerate Si–O antisymmetric stretch of the SiO_4 unit, which is split into two components at 843 and 825 cm^{-1} , and the intense $\nu_{as}SiOC$ band at 1099 cm^{-1} . The highest-energy band at 1195 cm^{-1} is assigned to a CH_3 in-plane rocking mode that picks up intensity by significant mixing with the $\nu_{as}SiOC$ vibration. The position and intensity of the $\nu_{as}SiO_4$ and $\nu_{as}SiOC$ bands in particular have been observed to be dependent upon the chemical environment of the TMOS molecule.

Hydrolysis Reaction. An immediate question to address is the location of TMOS in the microemulsion because, in contrast to the more commonly used TEOS, TMOS is soluble in both the hydrophobic and hydrophilic components of the microemulsion. The water-in-oil droplet is assumed to contain both water and the hydrophilic polyoxyether tail of the surfactant molecule and has been simulated by mixing water and polyethylene glycol 200 in a 6:1 molar ratio. The spectra of TMOS (0.1 M) in (a) an NP-5/cyclohexane/water microemulsion, (b) cyclohexane, and (c) polyethylene glycol 200 (aq) are compared in Figure 1. As discussed above, the spectra are referenced to the corresponding solvent without added TMOS. The $\nu_{as} Si-OC$ peak is located at 1099 cm^{-1} in both cyclohexane and the microemulsion, whereas it is found at 1062 cm^{-1} in the polyethylene glycol 200 (aq) solution, indicating that TMOS does not migrate preferentially

(11) Aldissi, M.; Henderson, S.; White, J. W.; Zemb, T. *Mater. Sci. Forum* **1988**, 27/28, 437.

(12) Webb, P. A.; Orr, C. *Analytical Methods in Fine Particle Technology*; Micromeritics: Norcross, GA, 1997; p 81.

(13) Ignatyev, I. S.; Lazarev, A. N.; Tenisheva, T. F.; Shchegolev, B. F. *J. Mol. Struct.* **1991**, 244, 193.

(9) Reetz, M. T.; Zonta, A.; Simpelkamp, J. *Biotechnol. Bioeng.* **1996**, 49, 527.

(10) Griffiths, P. R.; de Haseth, J. A. *Fourier Transform Infrared Spectrometry*; Chemical Analysis; John Wiley & Sons: New York, 1986; Vol. 83, p 194.

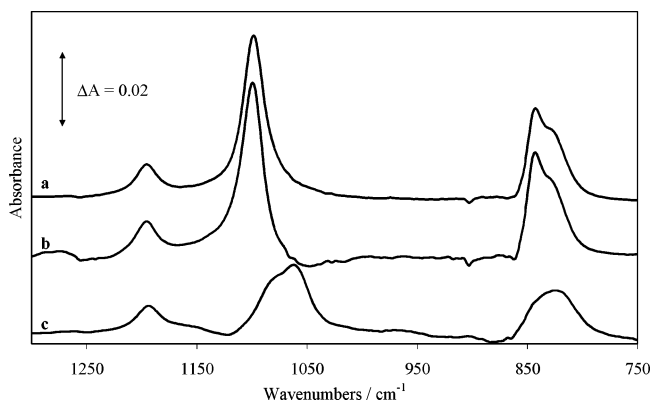


Figure 1. IR spectra ($1300\text{--}750\text{ cm}^{-1}$) of TMOS (0.1 M) in (a) an NP-5/cyclohexane/water microemulsion, (b) cyclohexane, and (c) polyethylene glycol 200 (aq).

into the water-in-oil droplet but is located mainly in the oil phase of the microemulsion.

Whereas the composition of the microemulsion (10:1 water/TMOS) indicates that hydrolysis rates should be moderate (<1 day), there are several complicating factors in using this information alone to predict hydrolysis rates. First, it is known that a certain amount of the water is bound to the surfactant polar groups and is not necessarily available to undergo reaction with TMOS. A previous study monitoring $\text{Ru}(\text{bpy})_3$ fluorescence in the same microemulsion system as studied here indicated that free water molecules were available only after the water/surfactant ratio exceeded 1.¹⁴ We have also noted the absence of the water vibrational mode at $\sim 700\text{ cm}^{-1}$ (not shown here) in the microemulsion containing 1:1 water/surfactant, which is clearly evident when the ratio is increased to 2:1, suggesting that the rotation of the water molecule is hindered in the 1:1 solution. Second, water is compartmentalized as water droplets of the microemulsion, whereas most of the TMOS resides in the oil phase. Diffusion of TMOS into the water droplets results in contact with ca. 15 M free water, assuming one-sixth is bound to the surfactant. Thus, in the presence of a suitable acid or base catalyst, hydrolysis should be very rapid indeed compared with that of a non-micellar system with similar TMOS and water concentrations.

The IR spectra following the addition of TMOS to both the acidic (pH 1.05) and basic (pH 10.85) microemulsions are shown in Figure 2a and b, respectively. Spectra of a corresponding non-micellar system in which TMOS and dilute acid (including the fluoride catalyst) have been reacted using the same concentrations (1.2 M water, pH 1.05; 0.12 M TMOS, 0.0012 M F^-) in acetonitrile are shown in Figure 3. The spectral region shown includes the main TMOS bands and the strongest vibrations of the evolving methanol and oxy-hydroxysilicate species. The difference in the hydrolysis rate under acidic and basic conditions is evident on comparing the intensity of the methanol $\nu(\text{C}\text{--}\text{O})$ band at 1028 cm^{-1} and the disappearing $\nu_{\text{as}}\text{SiO}_4$ bands at 843 and 825 cm^{-1} . After only several minutes, TMOS is 70% hydrolyzed in the microemulsion at pH 1.05, compared to $\sim 35\%$ at pH 10.85. After 30 min, TMOS is completely hydrolyzed in the acid system but only 70% hydrolyzed in the basic. Even after 60 min, a fraction ($\sim 10\%$) of TMOS remains unhydrolyzed in the base system. A comparison of hydrolysis rates at pH 1.05 for the microemulsion and non-micellar systems (Figure 2a and Figure 3) show that hydrolysis occurs more than an order of magnitude more rapidly in the microemulsion, with only 70% of TMOS hydrolyzed after 60 min in acetonitrile solution.

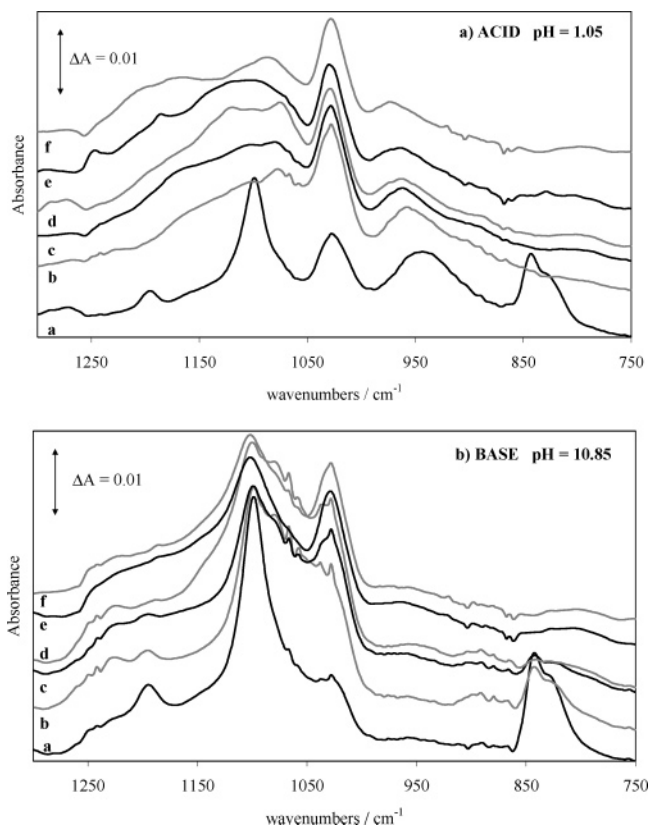


Figure 2. IR spectra ($1300\text{--}750\text{ cm}^{-1}$) following TMOS addition to (a) acidic (pH 1.05) and (b) basic (pH 10.85) microemulsions after stirring for (a) 2, (b) 30, (c) 60, (d) 120, (e) 240, and (f) 360 min.

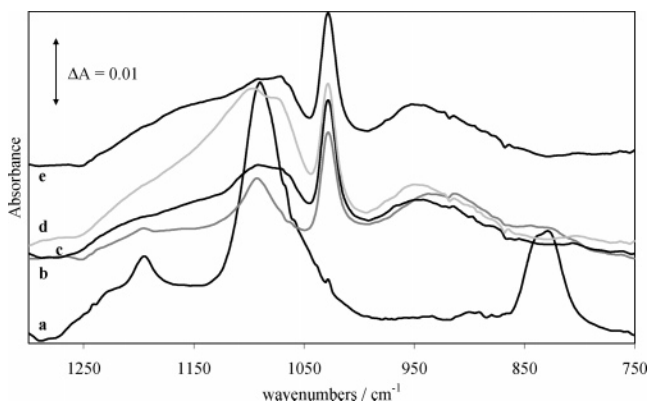


Figure 3. IR spectra ($1300\text{--}750\text{ cm}^{-1}$) following TMOS reaction with dilute acid (pH 1.05, contains fluoride) in acetonitrile after stirring for (a) 2, (b) 60, (c) 180, (d) 300, and (e) 360 min.

Condensation Reaction. After being stirred for 24 h, both acidic and basic microemulsions remained transparent and showed no signs of silica precipitation from the microemulsions. In contrast, a significant amount of solid had precipitated onto the container walls of the acetonitrile solution. It would appear that whereas the concentration of water in the reverse micelle clearly acts to enhance the hydrolysis kinetics of TMOS, the corresponding condensation processes are considerably altered by the presence of the surfactant.

Although not likely to give much information on long-range structure (such as provided by SAXS), a comparison of the IR spectra of the acid and base systems in Figure 2 show clear differences in Si–O bonding in the oxy-hydroxysilicates formed. First, the spectra in the base microemulsion show little variation with time after the addition of TMOS, aside from the growth of

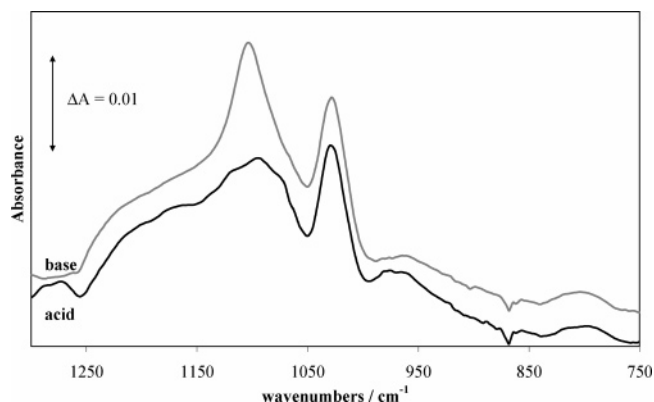


Figure 4. IR spectra (1300–750 cm^{-1}) of the acidic and basic microemulsions aged for 1 week after the addition of TMOS.

the methanol band at 1028 cm^{-1} and the eventual disappearance of the $\nu_{\text{as}}\text{SiO}_4$ bands at 843 and 825 cm^{-1} . The pronounced absorption band at 1100 cm^{-1} in the fully hydrolyzed samples is recognizable as the intense antisymmetric Si–O stretch of amorphous silica, which consists of a 3D network of corner-sharing SiO_2 tetrahedra.¹⁵ Because of fortuitous overlap with the $\nu_{\text{as}}\text{SiOC}$ band of TMOS, it is difficult to estimate when the species first appears in the spectrum, but it is clearly the major contributor to the spectrum recorded after 60 min because most of the TMOS has been hydrolyzed by this point. The weak higher-energy band at $\sim 1240 \text{ cm}^{-1}$ is commonly assigned as the corresponding longitudinal optical (LO) mode.¹⁶ In contrast to the base system, the spectra of the acidic microemulsion appear to undergo considerable evolution in structure over the 6 h shown here. The strong, broad absorption at $\sim 950 \text{ cm}^{-1}$ that appears immediately upon TMOS addition is only weakly observed in the base system and is assigned to the Si–O stretch of silanol groups.^{15,16} The base system at pH 10.85 is far away from the isoelectric point of silica (pH ~ 2), and thus silanols will be predominantly deprotonated, in effect shifting the band to higher energy. We would also expect a lower concentration of silanols on the reduced surface area of a more dense 3D network.

As opposed to the relatively sharp band formed at 1100 cm^{-1} after 1 h in the base system, there is a cluster of absorption maxima in the region from 1050 to 1250 cm^{-1} that change continually with time in the acid system. (The weak bands at 1273 and 1286 cm^{-1} are sporadically observed in association with an absorption band at 1728 cm^{-1} and are attributed to residual organic contaminants remaining on the ATR cell after cleaning.) After 6 h, however, the spectrum has stabilized to a main absorption band at 1087 cm^{-1} , with two higher-energy maxima (unresolved) at ~ 1170 and 1200 cm^{-1} . The spectrum after 24 h is very similar, with only a minor shift of the main band to 1095 cm^{-1} . In addition, there is a weak band growing slowly with time at 800 cm^{-1} in both the acid and base systems. This has been observed in both IR and Raman (at 830 cm^{-1}) studies of Si alkoxide hydrolysis and is attributed to Si–O–Si network formation.¹⁶

The absorption spectra of the acidic and basic microemulsions aged for 1 week after the addition of TMOS are shown in Figure 4. The microemulsions remained transparent, with no precipitation of silica. The shape of the group of Si–O stretching vibrations remains very similar to that of the spectra measured after 6 h, aside from somewhat more structure evident on the 1095 cm^{-1} band of the acid system. The main difference between the acid

and base systems is the relative intensity of the weak structure to the high-energy side of the main band at $\sim 1100 \text{ cm}^{-1}$, which is considerably more intense in the acid spectra. There has been some discussion about the assignment of these bands in the literature. Lazarev¹⁷ states that the appearance of bands in the range from 1150 to 1200 cm^{-1} is associated with the existence of straightened Si–O–Si bridges with a bond angle close to 180°. Lange has studied the effect of ion bombardment on the IR spectra of amorphous SiO_2 films and has attributed bands at 1165 and 1200 cm^{-1} to disorder in the oxide lattice.¹⁸ Linear Si–O chains are clearly highly disordered relative to normal tetrahedral SiO_2 bonding, so the two observations are not inconsistent with each other. The formation of linear siloxy chains is indeed predicted for acid-catalyzed condensation, in which condensation occurs via a protonated silanol, thus preferentially involving the more basic chain-end silicate species and giving rise to an open, randomly branched structure. Conversely, the deprotonation reaction in base-catalyzed condensation preferably involves a more highly condensed (more acidic) silanol, thus producing a relatively higher proportion of dense, highly branched Q^4 silica.⁶ SAXS measurements provide more information about the nature of evolving silicate structures. (See below.)

Comparing spectra of acidic microemulsions with and without added fluoride (not shown here) indicates that the fluoride acts to increase the kinetics of condensation significantly while slowing the initial hydrolysis slightly. The spectrum of the microemulsion without fluoride after 24 h resembles that of the microemulsion with fluoride after 4 h.

Summary. The in-situ FTIR measurements reveal that when introduced into the microemulsion, TMOS does not migrate preferentially into the reverse micelle but is located mainly in the oil phase. It slowly diffuses into the water pools where it is gradually hydrolyzed. At pH 1.05, this hydrolysis is complete after 30 min, whereas after the same time period at pH 10.85, 70% remains unhydrolyzed. Hydrolysis inside microemulsions occurs more than an order of magnitude faster than in typical single-phase sol–gel solutions at the same concentration. The condensation is also affected by both the presence of the surfactant and the pH of the water pools. The spectra of aged samples suggest the formation of linear, disorganized entities in acid and more condensed silicates in base in agreement with observations in homogeneous sol–gel solutions. The formation of the silica network appears to be more gradual in acid than in base, as expected again from the trends observed in bulk solutions.

SAXS. Small-angle scattering techniques provide a powerful method for characterizing reverse micellar systems and for in-situ investigations of the evolution of silica nanoparticles via condensation of the hydrolyzed species detected via FTIR. The approach used in this work involved modeling the scattering data (with intensities calibrated in absolute units) using a spherical form factor:

$$I(q, R_i) = \phi_i(\rho_i - \rho_{\text{solvent}})^2 \frac{4}{3} \pi R_i^3 F_{\text{sphere}}^2(q, R_i) \quad (1)$$

$$F_{\text{sphere}}(q, R_i) = \frac{3(\sin(qR_i) - qR_i \cos(qR_i))}{(qR_i)^3} \quad (2)$$

Here, ϕ_i is the volume fraction of the scattering species, $(\rho_i - \rho_{\text{solvent}})$ is the X-ray contrast difference between the scattering species and the continuous solvent phase, and R_i is the radius of the scatterers. The contrast difference between the solvent and

(15) Martínez, J. R.; Ruiz, F.; Vorobiev, Y. V.; Pérez-Robles, F.; González-Hernández, J. *J. Chem. Phys.* **1998**, *109*, 7511.

(16) Muroya, M. *Colloids Surf., A* **1999**, *157*, 147.

(17) Lazarev, A. N. *Vibrational Spectra and Structure of Silicates*; Consultants Bureau: New York, 1972; p 71.

(18) Lange, P. *J. Appl. Phys.* **1989**, *66*, 201.

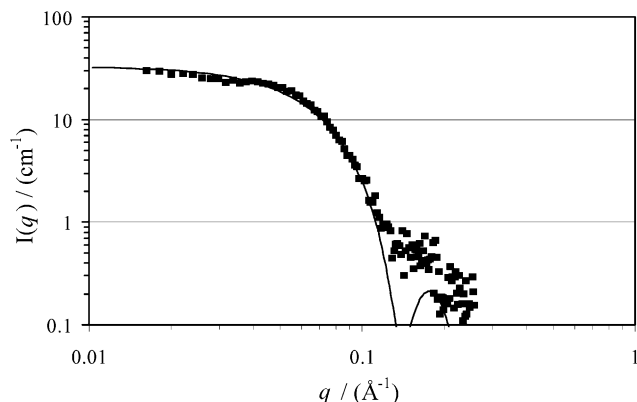


Figure 5. SAXS of fresh reverse micelles (■, base system), including the form factor fit (—).

hydrophobic domains is essentially negligible compared to that between the hydrophilic core and the solvent, and hence the scattering from the silica-free micellar system reflects the sizes and shape of the core region. The scattering from the silica-free micelles is illustrated in Figure 5, together with the results of a form-factor fit to deduce the apparent size of the scattering species. Because both $\Delta\rho$ and ϕ are fixed by the known composition of the system, the only variable fitting parameter is the value of R_{core} . The best fit is obtained using an equivalent radius of ca. 3 nm. This value is in good agreement with the 3.0 nm radius calculated from the measured aggregation number of ~ 220 for the surfactant in this system,^{5b} assuming densities for water and PEG chains within the core of 1.00 and 1.13, respectively. The hydrodynamic radius measured by dynamic light scattering is ca. 5 to 6 nm (not shown here), reflecting the contribution of the nonylphenyl chains (that have a fully extended length of ca. 1.5 nm) and associated solvent molecules to the overall size of the reverse micelles.

The formation of hydrolyzed silica species within the micellar system would be expected to complicate the small-angle scattering pattern significantly as a result of the multiple interfaces potentially present in the system (water–hydrocarbon, water–silica, and hydrocarbon–silica). However, the hydrophilicity of the silica surface suggests that it is unlikely that the silica species would reside in the hydrophobic domain, and hence only water–hydrocarbon and water–silica interfaces need to be considered. The contrast difference between silica and water is 5 times greater than that between water and hydrocarbon, suggesting that the scattering from the evolving silica species should be easily detected in the presence of the scattering from the reverse micelles, in spite of the lower volume fraction of silicates.

Base-Catalyzed Hydrolysis and Condensation. The SAXS data obtained in the base-catalyzed system are shown in Figure 6 as a function of reaction time.

Because absolute scattering intensities were obtained and the contrast terms and volume fractions are, in principle, fixed by the chemical composition of the system, it should be possible to fit the scattering data using the radii of the nanoparticles and micellar cores as the only variable parameters, together with polydispersity indices that reflect the finite width of the particle size distributions (mainly evident through the absence of the characteristic oscillations typically observed in the Porod-region scattering at high q for monodisperse species). However, initial attempts to fit the data using this approach were not successful, with significant least-squares differences observed between the best fits obtained and the experimental data. Hence, subsequent attempts to model the data were based on the assumption that a significant fraction of either the silica or surfactant (or both) was not contributing to the observed scattering. This could readily occur if not all of the alkoxide had reacted to produce silica or the integrity of the reverse micelles was disrupted by the formation of the nanoparticles within the micellar core. Thus, the scattering

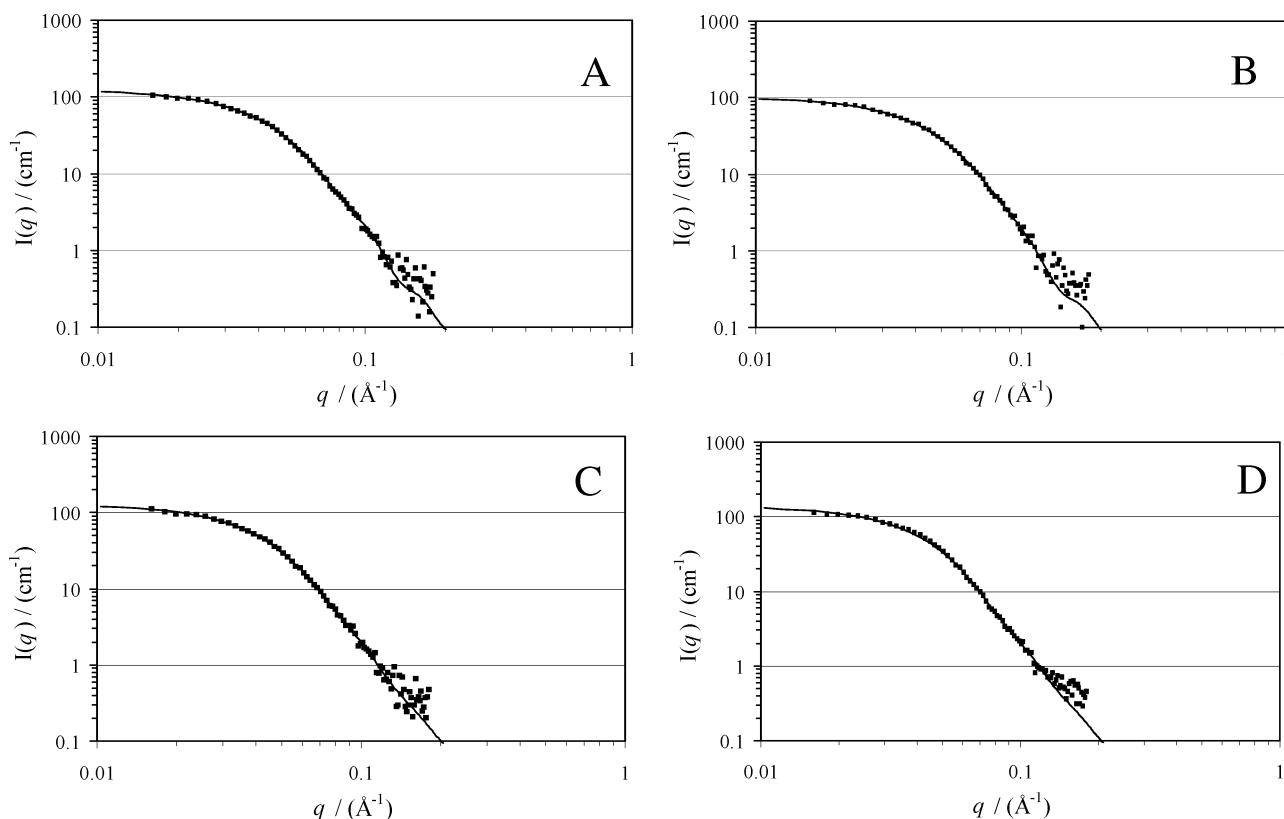


Figure 6. SAXS of reverse micelles containing evolving silica nanoparticles (■, base system) including form factor fits (—). (A) Fresh, (B) 90 min after initiating alkoxide hydrolysis, (C) 160 min after initiating hydrolysis, and (D) aged system.

Table 1. Nanoparticle and Reverse Micelle Radii and Polydispersity as a Function of Sol–Gel Processing Conditions

reaction time (hours)	system	micelle radius/nm (polydispersity)	% surfactant in micelles	nanoparticle radius/nm (polydispersity)	% silica in particles
fresh	pH 1.05, F ⁻	3.5 (1.1)	100	2.2 (0.1)	100
1	pH 1.05, F ⁻	3.4 (1.6)	100	2.6 (0.1)	100
3	pH 1.05, F ⁻	3.4 (1.7)	100	2.6 (0.1)	100
aged	pH 1.05, F ⁻				
aged	pH 1.05	3.6 (1.4)	100	2.6 (0.1)	100
fresh	pH 10.85	3.4 (1.5)	79	5.3 (1.4)	100
1.5	pH 10.85	3.5 (1.8)	88	5.6 (1.1)	100
2.5	pH 10.85	3.5 (2.2)	89	5.6 (1.9)	100
4	pH 10.85	3.6 (2.1)	85	5.6 (2.1)	100
aged	pH 10.85	3.7 (2.5)	100	5.5 (1.6)	100

model was modified by replacing the expected volume fractions of micellar cores and nanoparticles (ϕ_{core} and ϕ_{silica} , respectively) with apparent volume fractions obtained by including scaling factors, f_{core} and f_{silica} (where $0 \leq f_i \leq 1$), such that

$$I(q)_{\text{core}} = f_{\text{core}} \phi_{\text{core}} (\rho_{\text{core}} - \rho_{\text{solvent}})^2 \frac{4}{3} \pi R_{\text{core}}^3 F_{\text{sphere}}^2(q, R_{\text{core}}) \quad (3)$$

$$I(q)_{\text{silica}} =$$

$$f_{\text{silica}} \phi_{\text{silica}} (\rho_{\text{silica}} - \rho_{\text{solvent}})^2 \frac{4}{3} \pi R_{\text{silica}}^3 F_{\text{sphere}}^2(q, R_{\text{silica}}) \quad (4)$$

The apparent radii of the evolving silica nanoparticles and of the reverse micelles (obtained by least-squares fitting of spherical form factors with the radii of the micellar core and nanoparticles as variables) are summarized in Table 1, together with the corresponding values of f_{core} and f_{silica} and the size polydispersity indices. The data at all reaction times could be modeled by assuming that all of the silica in the systems was located in the particles (i.e., $f_{\text{silica}} = 1.0$) and that the particles are “dense” objects; that is, their scattering length density is appropriate for that of amorphous silica with essentially no porosity. In addition, the apparent radius and polydispersity of the nanoparticles does not change significantly with time, with radii of 5.3 to 5.6 nm observed for reaction times exceeding 90 min. However, it is evident that the nanoparticles are somewhat larger than the core of the reverse micelles (3 nm) in which the sol–gel chemistry was initiated, clearly indicating that the silica particles cannot be accommodated within the micellar core. Because no precipitation was observed, this suggests that the nanoparticles may be stabilized in the system by a layer of adsorbed surfactant, which provides a steric barrier against aggregation.

The apparent radii, polydispersity, and variations in f_{core} with reaction time for the reverse micelles are also summarized in Table 1. Both the micelle size and polydispersity appear to increase slightly with increasing reaction time, reflecting a minor decrease in the surfactant/water ratio with increasing reaction time. This result was initially unexpected because water is consumed during the sol–gel reaction, and hence an increase in the surfactant/water ratio would be anticipated. However, the data in Table 1 also suggests that 10–20% of the total surfactant in the system is no longer located within the reverse micelles after the sol–gel chemistry is initiated. This result is consistent with the proposed stabilization of the silica nanoparticles in the system through the formation of a water/surfactant layer on the surface of the nanoparticles.

Acid-Catalyzed Hydrolysis and Condensation. The SAXS data obtained in the acid-catalyzed system for selected systems (with and without added fluoride) are shown in Figure 7 as a function of reaction time, and the corresponding nanoparticle sizes and polydispersities are summarized in Table 1. A number of significant differences between the structural evolution of the

nanoparticles under acidic and basic conditions are immediately evident. In contrast to the base-catalyzed system, the majority of silica and surfactant present in the systems contributes to the observed scattering in the acid-catalyzed system, suggesting that most of the alkoxide has hydrolyzed (as revealed by FTIR) and has undergone significant condensation within the first 2 h of reaction. In addition, a majority of the micelles appear to remain intact during the evolution of silica nanoparticles under acid-catalyzed conditions.

The size of the silica nanoparticles in the acid-catalyzed system is significantly smaller than that observed under base-catalyzed conditions (Table 1), with radii of 2.2 (fresh) to 2.6 nm (aged) observed in the acid-catalyzed systems, together with very low polydispersity indices. These dimensions are smaller than that of the reverse micelles, suggesting that the nanoparticles in the acid-catalyzed system may be retained within the micellar core, in contrast to the base-catalyzed system where the larger nanoparticles are stabilized against aggregation by sorption of (hydrated) surfactant on the particles’ surfaces.

Unlike the base-catalyzed systems, where good form-factor fits were obtained in absolute units at all reaction times and over

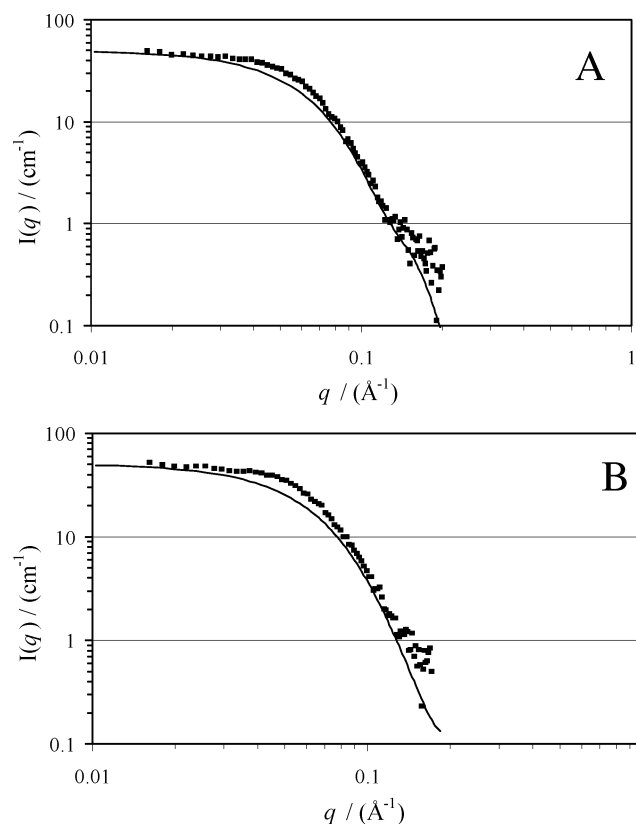


Figure 7. SAXS of reverse micelles containing evolving silica nanoparticles (■, acid system) including form factor fits (—). (A) Fresh and (B) 180 min after initiating alkoxide hydrolysis.

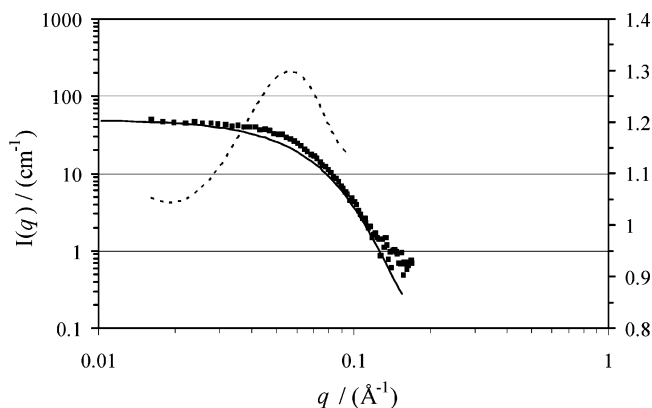


Figure 8. Apparent $S(q)$ function (---) obtained by dividing SAXS of evolving silica particles in the acid-catalyzed system, 180 min after initiating hydrolysis (■), by the corresponding fitted $P(q)$.

the entire q range investigated, the corresponding acid-catalyzed systems yielded significantly poorer fits at intermediate q (0.04 – 0.1 \AA^{-1}), although reasonable fits were obtained at low and high q . These results suggest that the observed scattering at intermediate q cannot be modeled by fitting a simple spherical form factor and that the contribution of structure-factor effects ($S(q)$) must also be considered in the acid-catalyzed system:

$$I(q) = S(q) P(q) \quad (5)$$

In the base-catalyzed system, $S(q) = 1$ over the q range investigated. However, under acid-catalyzed conditions, the values of $S(q)$ appear to exceed unity at intermediate q . Variations in the apparent structure factor with q were extracted at each time point by dividing the experimental data by the fitted form factor, as illustrated in Figure 8. These data reveal a peak in $S(q)$ at around $q = 0.05 \text{ \AA}^{-1}$ (equivalent Bragg distance of 120 – 130 \AA), with the intensity of the peak increasing with increasing reaction time. This size is comparable to that of the reverse micelles, as observed by dynamic light scattering, and reflects the development of longer-range organization in the nanoparticle–reverse micelle system with increasing reaction time. It is interesting that reasonable fits to the scattering data could not be obtained in the aged fluoride-containing, acid-catalyzed system, indicating that structure-factor effects (and the associated organization of the system) dominated the simple form-factor contributions of the individual nanoparticles and reverse micelles to the observed scattering.

These comparisons further highlight the significant differences observed by FTIR in the structural evolution of silica nanoparticles in reverse micelles under acid- and base-catalyzed conditions. Apart from the expected differences in hydrolysis and condensation rates, the nanoparticles obtained in the acid-catalyzed system (where hydrolysis is rapid and condensation is the rate-limiting step) are more uniform in size (low polydispersity index) and form an ordered micelle–nanoparticle structure that exhibits sufficient long-range order to generate a peak in the scattering at $q \approx 0.05 \text{ \AA}^{-1}$.

Particle Morphology and Internal Structure. Nitrogen adsorption analysis indicates that the internal structure of the particles is strongly affected by the pH of the water droplets. The particles formed in an acidic environment exhibit a type IV isotherm (Figure 9a) with a strong microporous component, which is reflected by a pore size distribution centered around 1 nm (Figure 9b) and a relatively large surface area ($510 \pm 8 \text{ m}^2/\text{g}$). In contrast, the particles synthesized in base exhibit an isotherm with a strong mesoporous contribution. Figure 9b reveals a pore size distribution with most of the pores larger than 15 nm , which

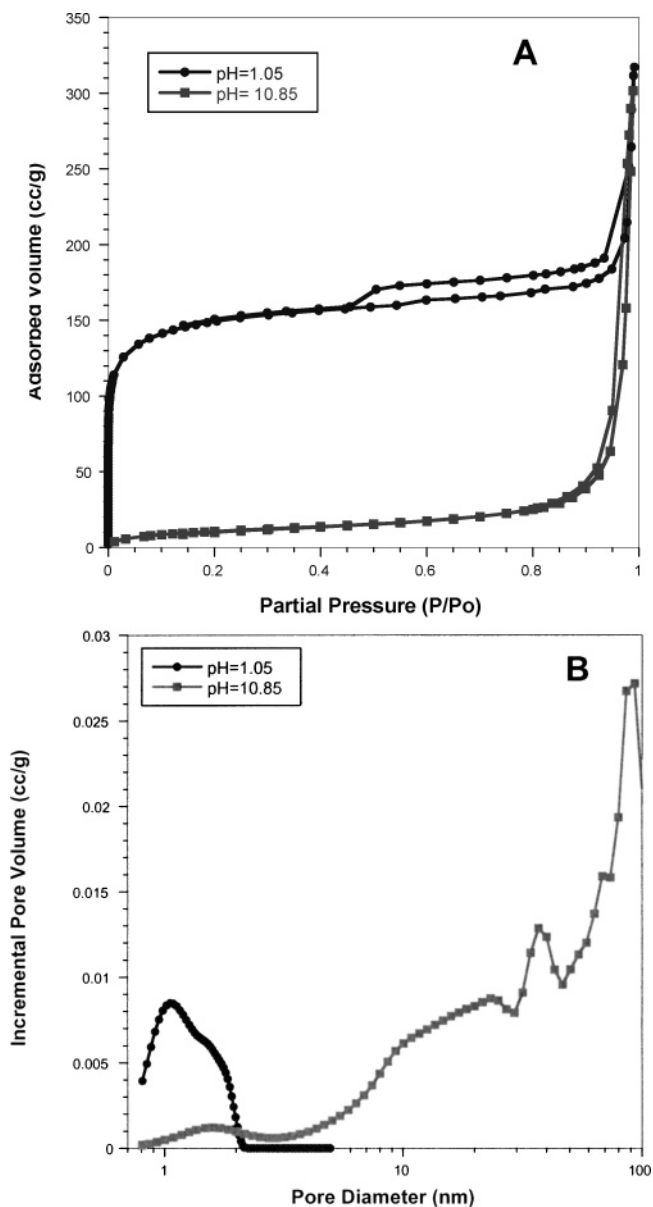


Figure 9. (A) Nitrogen adsorption isotherm and (B) pore size distribution of particles synthesized in acid (●) and in base (■).

is the diameter of the particles. This suggests that these large pores relate to the interparticle gaps rather than the internal porosity of the particles. The small volume of pores ($<10 \text{ nm}$) combined with a relatively low surface area ($87 \pm 0.4 \text{ m}^2/\text{g}$) confirms the dense nature of the particles observed by FTIR and SAXS. Indeed, dense silica particles of 11 nm diameter should exhibit a surface area that is 3 times greater than this. In contrast, the high microporosity and surface area of the particles synthesized in acid suggest a more open and disorganized structure.

Discussion

Mechanisms of Nucleation and Growth in Microemulsions.

The growth of particles in microemulsions is governed by the same mechanisms as colloidal suspensions: nucleation and growth of particles occur by either ripening aggregation or coagulation.

Nucleation in water-in-oil microemulsions takes place when the concentration of hydrolyzed precursors present in the reverse micelle droplets exceeds the nucleation threshold C_n . The only difference as compared to classical colloidal suspensions is that

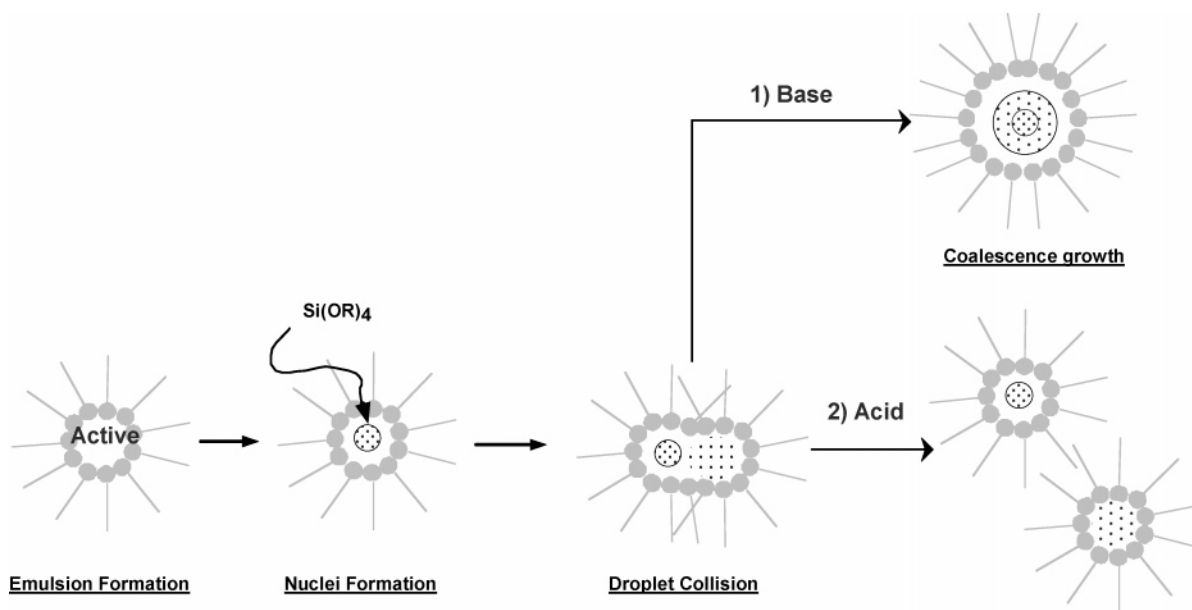


Figure 10. Proposed mechanism for particle formation under acidic and basic conditions.

in microemulsions the solution is compartmentalized inside small droplets. Thus, the concentration of hydrolyzable monomers can differ from water droplet to water droplet. In other words, hydrolysis generates monomers that form nuclei when their concentration per droplet is larger than C_n . On the basis of these considerations, the number of nuclei will increase with rapid hydrolysis and condensation. Another specific characteristic of microemulsions is that the droplets exchange their core contents during collision. An increase in the rate of intermicellar exchange can induce a redistribution of the hydrolyzed monomers before supersaturation reaches the nucleation threshold. Thus, increasing the collision of micelles can lead to a decrease in the nucleation rate.

As for aqueous colloidal suspensions, particle growth follows nucleation. The water droplets can be viewed as microreactors where particle growth takes place by the addition of hydrolyzed monomer to the nuclei. Thus, the higher the number of nuclei, the smaller the resulting particles. Similarly, for a fixed number of nuclei, the higher the supersaturation in the pool, the larger the resulting particles. As discussed above, microemulsions are dynamic systems, and the microemulsion droplets collide constantly with one another, exchanging the content of their aqueous core in the process. Growth can then take place by the collision of droplets containing solid nuclei or particles with undersaturated droplets containing only hydrolyzed monomers. In other words, growth can take place by the consumption of unsaturated micelles (in a process akin to coalescence). Thus, the final particle size increases with the number of collisions or micellar exchanges.

Base catalysis of sol–gel reactions promotes hydrolysis, condensation, and, more importantly, dissolution. At pH 10.85, FTIR reveals a relatively modest hydrolysis rate that results in relatively small and heterogeneous nucleation (i.e., the nucleation varies from micelle to micelle). This leads to the production of a fairly inhomogeneous and polydisperse system. Rapid condensation results in quick consumption of all of the precursors inside the micelles and the formation of a dense silica structure. Further growth can take place by aging and scavenging of the contents of other droplets. A high dissolution rate ensures the production of spherical and dense particles by the ripening of potential aggregates formed during the collision of droplets containing nuclei (Figure 10). During this process, the particles

outgrow the original droplets (as observed by SAXS) but are maintained in suspension by a layer of adsorbed surfactant (i.e., 20% of the total surfactant not present in the micelles, Table 1).

Acid catalysis, in contrast, promotes hydrolysis but hinders both condensation and dissolution reactions. Consequently, for the microemulsion synthesis of silica particles using acid catalysis, a lot of nuclei are generated quickly, but very small growth is observed. This leads to the formation of significantly smaller but more homogeneous particles as observed by SAXS. In fact, no solid particles are observed in acid-catalyzed microemulsions even after aging for 48 h. A condensation catalyst such as fluoride is necessary for the production of solid particles. The finding by SAXS that the majority of micelles remain intact during the formation of silica nanoparticles suggests that, in contrast to base catalysis, no coalescence takes place between the droplet contents during intermicellar collisions (Figure 10). The particles grow to fill the micelle core by slowly consuming all of the hydrolyzed precursors present in its pool. The gradual evolution of both the FTIR and SAXS patterns during aging confirms this gradual evolution of the structure inside the micellar droplets.

Conclusions

An in-situ study of the formation of silica nanoparticles intended for drug-delivery applications has enabled a clearer understanding of the reaction kinetics inside the microemulsion and the microstructural dependence on the different pH conditions used. In summary, TMOS diffuses from the oil phase of a H₂O/NP5/cyclohexane microemulsion into the internal water droplets, resulting in hydrolysis at various rates depending on the pH. At pH 1.05, this hydrolysis is complete after 30 min, whereas after the same time period at pH 10.85, 70% remains unhydrolyzed. Under acidic conditions, linear, disorganized entities form slowly inside the water droplets, resulting in high surface area, microporous 5 nm particles. In contrast, tetrahedral silica is formed at pH 10.85, outgrowing the water droplets as they collide and coalesce, resulting in dense, nonporous 11 nm particles.

Acknowledgment. We thank Alexandra Bush for assistance with the SAXS data collection and Elizabeth Drabarek for the porosity measurements.

LA0624283